

# Multiscale Optimization of 3D-Printed Beam-Based Lattice Structures through Elastically Tailored Unit Cells

Oliver Schwahofer,\* Sascha Büttner, Johannes Binder, David Colin, and Klaus Drechsler

Herein, a numerical multiscale tool is developed to design 3D periodic lattice structures. The work is motivated by the high design freedom of additive manufacturing technologies, which enable complex multiscale lattice structures to be printed. A finite-element-based free-material optimization method is used to determine the ideal orthotropic material properties of a 3D macrostructure space. Subsequently, a population-based algorithm is established to design optimized microscopic lattice unit cells with the desired structural properties. The design variables are the coordinates of lattice skeleton nodes defined within the 3D lattice unit cell space, and the connectivities between them resulting in a truss skeleton. For the calculation of the mechanical properties of the individual lattice cells, an effective Timoshenko beam-based finite element calculation method is developed. The macroscale structure can be constructed by periodically filling the domain with the customized unit cell representing a metamaterial. The method is demonstrated by 3D beam problems with compliance constraints. These macroscopic demonstrators of the developed lattice structures were also 3D-printed. The benefit regarding the weight-specific structural performance is validated through benchmarking with periodic lattice design solutions using well-known standard lattice cells.

## 1. Introduction

Additive manufacturing enables complex lattice structures, which would not be feasible with other manufacturing techniques, to be easily produced. In this article, the design of periodic lattice structures, which can be built together by stacked repeating unit cells, is targeted. One microscale unit cell represents a specific metamaterial with the option of complex anisotropic elastic and elastoplastic properties. In this article, only elastic stiffness is researched, but the extension of the developed framework to nonlinear mechanics such as yield strength and energy absorption is in

progress. This serves as one of the reasons why metaheuristic optimization methods<sup>[1–4]</sup> were selected instead of traditional sensitivity-based algorithms,<sup>[5,6]</sup> even though there are some successful implementations for unit cell optimization using derivative-based methods.<sup>[7–9]</sup>

The traditional design of periodic lattice structures happens through the commonly used standard cells such as body- and face-centered cube, octet cell, or honeycomb. In such a framework, the infill rate or the predefined geometric parameters such as diameter or thickness are optimized or adjusted to targeted structural requirements. In this work, the main motivation is designing lattice structures through individually tailored lattice unit cells, which represent a metamaterial that perfectly matches the requirements of a macroscopic problem. Such topology-optimized microcells can outperform the standard cell, and due to the high design freedom of additive manufacturing techniques, such complex structure is


printable. The novel approach is extendable to a multiobjective formulation composed of multiphysical design responses such as thermal or acoustic properties or energy absorption. This would enable to design multifunctional smart metamaterials in the form of microstructures, which serves as the main motivation of the work.

Research on periodic cellular materials has a long history, but its importance has increased in recent years due to advanced manufacturing techniques. Basic lattice and foam unit cells and corresponding mechanical capabilities are summarized in refs. [10–12] For the homogenization of mechanical properties analytical,<sup>[12]</sup> numerical,<sup>[13,14]</sup> and experimental methods<sup>[15]</sup> may be used. These techniques enable the approximation of the effective structural properties of a beam-based lattice representative volume element (RVE). In this work, finite element-based homogenization is used for the elastic characterization of the unit cells. A low-fidelity Timoshenko beam-based model was established to model the truss-based lattice geometry. This method replaces the traditional, but computationally more expensive, solid tetrahedral or hexahedral models. Numerical homogenization of lattice cells through elastic beams has been partly covered in the literature. 2D models are common in research, first published by Tollenaere and Caillerie.<sup>[16]</sup> Further studies were carried out by Reis et al.,<sup>[17]</sup> Vigliotti,<sup>[18–20]</sup> and Park and Rosen.<sup>[21]</sup>

Ground structure optimization through a population-based algorithm was first established by Zhang.<sup>[22]</sup> Further, truss-based problems were approached through genetic and evolutionary

---

O. Schwahofer, S. Büttner, J. Binder, D. Colin, K. Drechsler  
Chair of Carbon Composites  
Technical University of Munich  
Boltzmannstr. 15, 85748 Garching, Bayern, Germany  
E-mail: oliver.schwahofer@tum.de

 The ORCID identification number(s) for the author(s) of this article can be found under <https://doi.org/10.1002/adem.202201385>.

© 2022 The Authors. Advanced Engineering Materials published by Wiley-VCH GmbH. This is an open access article under the terms of the Creative Commons Attribution-NonCommercial-NoDerivs License, which permits use and distribution in any medium, provided the original work is properly cited, the use is non-commercial and no modifications or adaptations are made.

DOI: 10.1002/adem.202201385

methods by Su et al.<sup>[23]</sup> and Giger et al.<sup>[24]</sup> Bujny et al.<sup>[25,26]</sup> and Raponi<sup>[27,28]</sup> researched energy absorption problems through metaheuristic methods. All of the mentioned frameworks were implemented in a macroscopic single-scale domain. In this article, a metaheuristic method is implemented on the microlevel for the optimization of unit cells, and they are built together to form a macroscale structure. For the derivation of the target material properties on the macroscale, a 3D sensitivity-based free-material optimization method is used.<sup>[29–31]</sup> Further, free-material numerical schemes are presented in.<sup>[32–34]</sup> A similar method is implemented in certain multiscale lattice-based methods.<sup>[35,36]</sup>

Multiscale lattice design methods were introduced by several studies. A review of structural optimization trends from the field of periodic lattice structures is summarized by Pan et al.<sup>[37]</sup> A truss diameter-based method is presented by Gorgularslan et al.,<sup>[38]</sup> where the members of predefined standard cells are optimized. In the work of Marschall et al.,<sup>[14]</sup> a multi-cell-graded lattice cell method is implemented using predefined standard cells. Another graded lattice approach is using the body-centered cube to map the structural properties by varied member diameters. The nonuniformly graded anisotropic cells form the macrostructure achieving good lightweight performance.<sup>[35,39]</sup> Other methods of two-scale elastic lattice structure design were explored through high-fidelity optimization considering material property gamut by Chen et al.<sup>[40]</sup> and Zhu et al.<sup>[41]</sup> In this article, a three-dimensional multiscale method is presented where the microstructure is tailored through a population-based algorithm allowing a multiobjective microscale design formulation to solve macroproblems.

## 2. Methodology

This work focuses only on the numerical simulation and design optimization of periodic lattice structures. The presented approach is independent of the choice of the printed material, as well as of manufacturing technology. Therefore, a homogeneous and isotropic reference material, which is independent of any 3D printing process-induced effects on the material quality and properties, is assumed. In this article, only lattice cells with triple symmetry are considered. An exemplary unit structure is demonstrated in **Figure 1**.

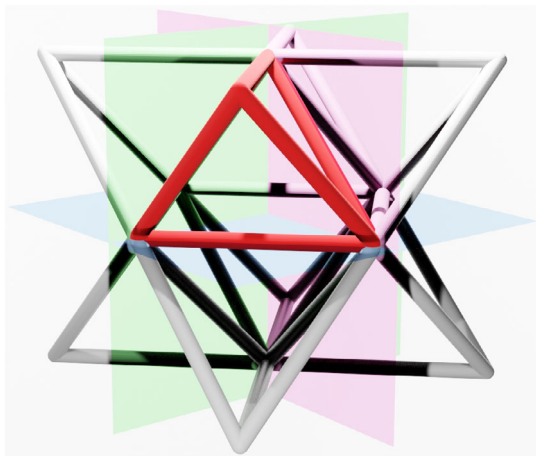


**Figure 1.** 1/8th Cell mirrored across the three centre planes.

### 2.1. Homogenization Method

A repeating unit cell of the whole structure, which is commonly referred to as representative volume element (RVE), can be represented through its homogenized structural properties. In this work, only beam-based lattice unit cell geometries are optimized.

For the estimation of the mechanical properties of the lattice unit cell, a reduced-order numerical homogenization tool was developed. A truss-based lattice unit cell geometry is modeled by Timoshenko elastic beams. The homogenization method consists of two steps. First, the truss skeleton is refined by multiple beam elements. Second, the junction beams are selected for stiffness upscaling to model the elastic effects of material concentration near the junction point of one or more trusses. During this reinforcement step, the closed angle between the trusses as well as the orientation vector with respect to the loading direction are considered. The reinforced elastic parameter ( $E_{\text{reinf}}$ ) is modeled as a function of these two properties. The parameters of the models are calibrated through a few unit cell analyses, where the homogenized properties of the beam-based calculation are compared with the results of solid-meshed analyses. The validity range of the Timoshenko beam-based modeling framework in terms of slenderness is derived through geometric parameter variation of the calibration cells.

The beam-based reduced-order homogenization method is summarized in **Figure 2**.

Periodic boundary conditions are then assigned to the beam model, and the homogenization can take place in the six principle strain directions of the cell. The calculation is performed in an Abaqus–Python framework, based on the homogenization tool easyPBC.<sup>[42]</sup> Due to the beam-based FE model, additional rotation boundary conditions are assigned to the opposing surfaces of the unit cell to capture the effect of the periodically adjacent cells. The outputs of the homogenization are the anisotropic elastic properties of the modeled lattice unit cell.

### 2.2. Lattice Unit Cell Optimization

The quick homogenization scheme established in Section 2.1 is integrated into the population-based unit cell optimization framework (**Figure 3**). The two-step method first uses a genetic algorithm (GA) to generally optimize the unit cell topology. In this context, topology is used to only describe the way the separate nodes are connected, without considering the specific position of the nodes. The result of the GA ideally is an optimal topology, with suboptimal node positions being permissible. The design variables are the nodal locations and the connectivities (trusses) between them.

Then, a reduced degree of freedom optimization is done posterior to the main GA loop in the form of a PSO algorithm, which will find the optimal node position for the specific input topology. The posterior PSO loop can be treated as a shape optimization of the prior topology optimization in the GA. The approach is implemented in a Python script responsible for genetic operations and optimization, evaluating each genotype through the beam-based Abaqus–Python interface (Section 2.1).

The optimization starts with an initial random population. The designs of the cells are controlled through various geometric

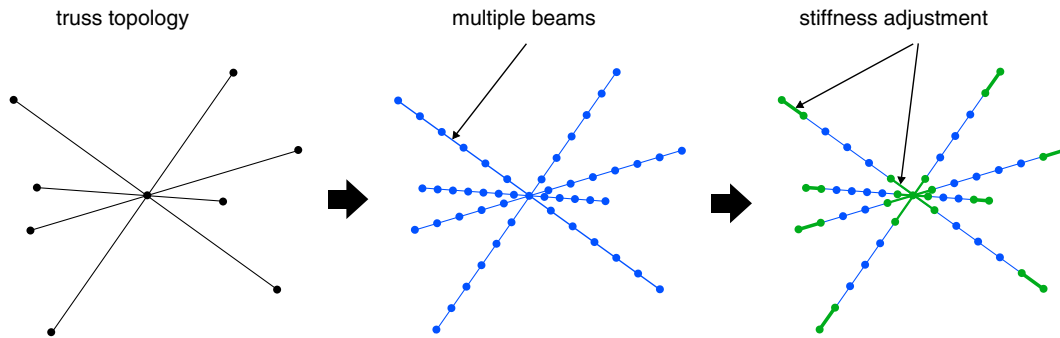


**Figure 2.** Discretization and reinforcement of a truss-based lattice.

settings (truss diameter, unit cell dimensions, maximum number of nodes) and geometric hard constraints (minimum connection length, minimum node-to-node distance, minimum connection-to-connection distance, and minimum connection-to-node distance). These setup options help to control the design complexity, the infill ratio, and the slenderness of the unit cell, which is crucial for an accurate Timoshenko-based approximation.

During the GA, mating and mutation operations are coded for the evolution of the cell topologies. The optimization objective is weight-specific stiffness (Equation (1)) in the main direction. That is combined with the cost functions of the other directional stiffness ratios (Equation (2)) and the number of cell connections ( $c_{con}$ ) to reduce topology complexity.

$$f_{\text{stiffness}} = \frac{E_1}{\rho_{\text{infill}}} \quad (1)$$

$$c_{\text{ratio},i} = \begin{cases} \left(1 + \frac{E_j/E_k - r_i}{r_i} \times w_i\right)^3 & E_j/E_k > r_i \\ \left(1 + \frac{r_i - E_j/E_k}{E_j/E_k} \times w_i\right)^3 & E_j/E_k \leq r_i \end{cases} \quad (2)$$

As an alternative, the cost function of the other directional stiffness values can be also formulated through their direct magnitude (Equation (3)), instead of the dimensionless ratio with respect to the dominant optimization direction as in

Equation (2). In the case of ratio-based Equation (2), the cost function is insensitive to the stiffness magnitudes. The ratios are formulated with respect to the dominant stiffness property ( $E_k$ ).

$$c_{\text{direct},i} = \begin{cases} \left(1 + \frac{E_i - E_{\text{target},i}}{r_i} \times w_i\right)^3 & E_i > E_{\text{target},i} \\ \left(1 + \frac{E_{\text{target},i} - E_i}{E_i} \times w_i\right)^3 & E_i \leq E_{\text{target},i} \end{cases} \quad (3)$$

The overall fitness is combined together in Equation (4). Of course, the fitness function can be also formulated with the help of the magnitude-based cost formulation ( $c_{\text{direct},i}$ ) from Equation (3).

$$f_{\text{complete}} = \frac{f_{\text{stiffness}}}{c_{\text{con}} \times c_{\text{ratio1}} \times c_{\text{ratio2}}} \quad (4)$$

Similar cost functions are also implemented for the control of the shear modulus and Poisson's ratios as well.

### 2.3. Integration to Structural Problems

To be able to integrate the lattice cells with tailored elasticity from Section 2.2, a method was established to derive the optimal meta-material parameters of the 3D macrodomain to be designed in the form of a tailored lattice cell. Free-material optimization

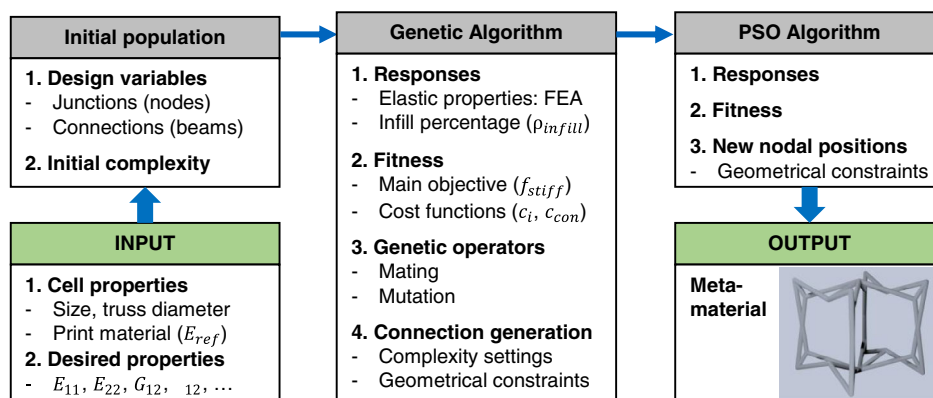


**Figure 3.** Unit-cell tailoring framework through population-based algorithm.

(FMO) is a powerful approach for structural optimization in which the design parametrization allows the entire elastic stiffness tensor to vary freely at each point of the design domain. The only requirement imposed on the stiffness tensor lies in its mild necessary conditions for physical attainability in the context that it has to be symmetric and positive semidefinite.<sup>[43]</sup>

In this article, two approaches are separated. The single-cell method treats every finite element of the whole macrodomain as a uniform material. The multicell approach allows the combination of various lattice unit cells representing different metamaterials.

### 2.3.1. Single-Cell Approach

The response that is used for the formulation of the objective is stated in Equation (5). The design variables are summarized in Equation (6). The Poisson's ratios can be design variables, as well as they can be kept fixed during the free-material optimization, and therefore excluded from the design variables. In that case, only the six stiffness moduli are varied, and Poisson's ratios can be a user-defined constant value. The Poisson's ratios might be excluded from the FMO process, as they are usually less sensitive to the overall stiffness performance of the cell. Furthermore, it is more challenging to target Poisson's ratios in the unit cell optimizer. For that reason, it is recommended to run the unit cell optimizer without Poisson's ratio targets.

$$f(E_1, E_2, E_3, G_{12}, G_{23}, G_{31}) = E_1 + E_2 + E_3 + G_{12} + G_{23} + G_{31} \quad (5)$$

$$X = \begin{pmatrix} E_1 \\ E_2 \\ E_3 \\ \nu_{12} \\ \nu_{23} \\ \nu_{31} \\ G_{12} \\ G_{23} \\ G_{31} \end{pmatrix} \quad (6)$$

To fulfill the stability criterion of the material, the stability constraints from Equation (7) must be activated during the optimization.

$$\begin{aligned} q_{\text{stab,a}} &= E_1 - E_2 \nu_{12}^2 \geq 0 \\ q_{\text{stab,b}} &= E_2 - E_3 \nu_{23}^2 \geq 0 \\ q_{\text{stab,c}} &= E_3 - E_1 \nu_{31}^2 \geq 0 \\ q_{\text{stab,d}} &= 1 - \nu_{12} \nu_{21} - \nu_{23} \nu_{32} - \nu_{13} \nu_{31} - 2\nu_{21} \nu_{32} \nu_{13} \geq 0 \end{aligned} \quad (7)$$

The objective (Equation (8)) of the macrooptimization is the minimization of the response from Equation (5), which is the sum of the six principal elastic properties. This is based on the assumption that lower stiffness targets can be achieved through less material, which leads indirectly to a minimum volume design. The macroproblem is subjected to a compliance constraint to formulate the optimization problem that is stated

in Equation (9). Here,  $U_c$  indicates the desired maximum admissible displacement at certain locations of the domain as a macroscale stiffness constraint.

$$\min_X f(X) \quad (8)$$

$$g_{\text{comp},i}(X) = U_i(X) - U_{c,i} \geq 0 \quad (9)$$

$$\begin{pmatrix} E_{1,\min} \\ E_{2,\min} \\ E_{3,\min} \\ \nu_{12,\min} \\ \nu_{23,\min} \\ \nu_{31,\min} \\ G_{12,\min} \\ G_{23,\min} \\ G_{31,\min} \end{pmatrix} \leq \begin{pmatrix} E_1 \\ E_2 \\ E_3 \\ \nu_{12} \\ \nu_{23} \\ \nu_{31} \\ G_{12} \\ G_{23} \\ G_{31} \end{pmatrix} \leq \begin{pmatrix} E_{1,\max} \\ E_{2,\max} \\ E_{3,\max} \\ \nu_{12,\max} \\ \nu_{23,\max} \\ \nu_{31,\max} \\ G_{12,\max} \\ G_{23,\max} \\ G_{31,\max} \end{pmatrix} \quad (10)$$

During the optimization of the material parameters, the design variables are limited between a minimum and maximum value. The upper bounds of the design variables should be defined based on an approximated maximum achievable stiffness limits. If the macroscopic stiffness problem cannot be solved within the prescribed limit of elastic constants, either stiffer printing material or a more complex and less slender unit cell design is advised. The maximum achievable stiffness and the approximated infill rate of the tailored cell can be controlled through geometric ( $d_{\text{truss}}$ ) and complexity (minimum connection length, minimum node-to-node distance, maximum number of nodes, maximum number of connections) settings, which should be selected according to the targeted stiffness values.

### 2.3.2. Multicell Approach

As a second approach, multiregion-free material was established. In this sense, every element of the design domain is an independent optimization design variable ( $X_i$ ) and every unit cell converges to an individual metamaterial in terms of elastic properties. This modifies the objective function of the problem slightly, as seen in Equation (11), where  $i$  indicates the element index of the whole design domain.

$$\min_X F(X) = \sum_i^m f_i(X_i) \quad (11)$$

Directly after the free-material optimization, a filtering algorithm takes care of clustering the elements into  $n_c$  subgroups. Afterward, a postoptimization is executed on the elastic properties of the clustered metamaterials. This process results in  $n_c$  different metamaterials being constructed through the unit cell tailoring tool from Section 2.2.

To cluster cells with similar stiffness properties into different groups, the K-Means algorithm from the Python scikit-package<sup>[44]</sup> is used in this work. The K-Means algorithm divides the data points into  $k$  distinguishable groups according to Equation (12). For this algorithm, it is necessary to specify the desired number of clusters ( $n_c$ ) in advance. The flowchart of the clustering algorithm can be seen in Figure 4.

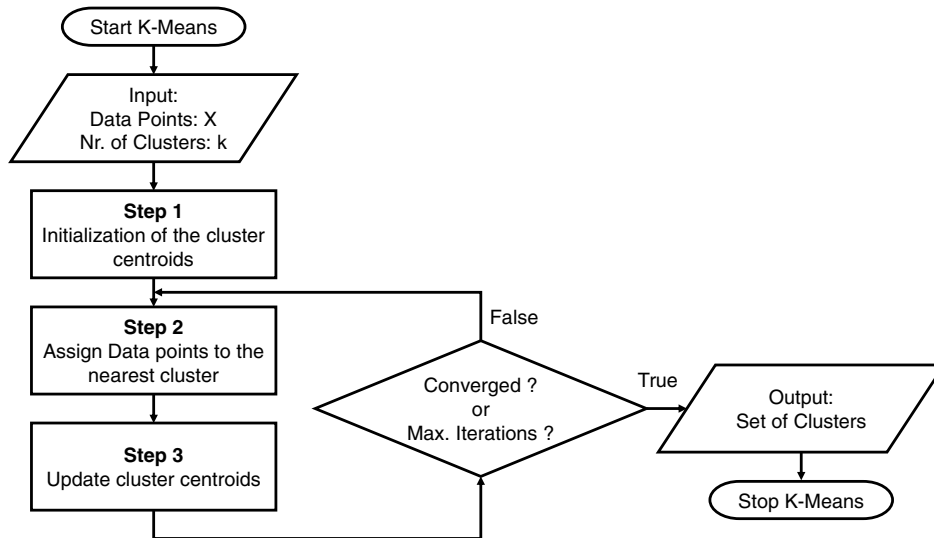


Figure 4. Flowchart of data clustering using the K-Means algorithm.

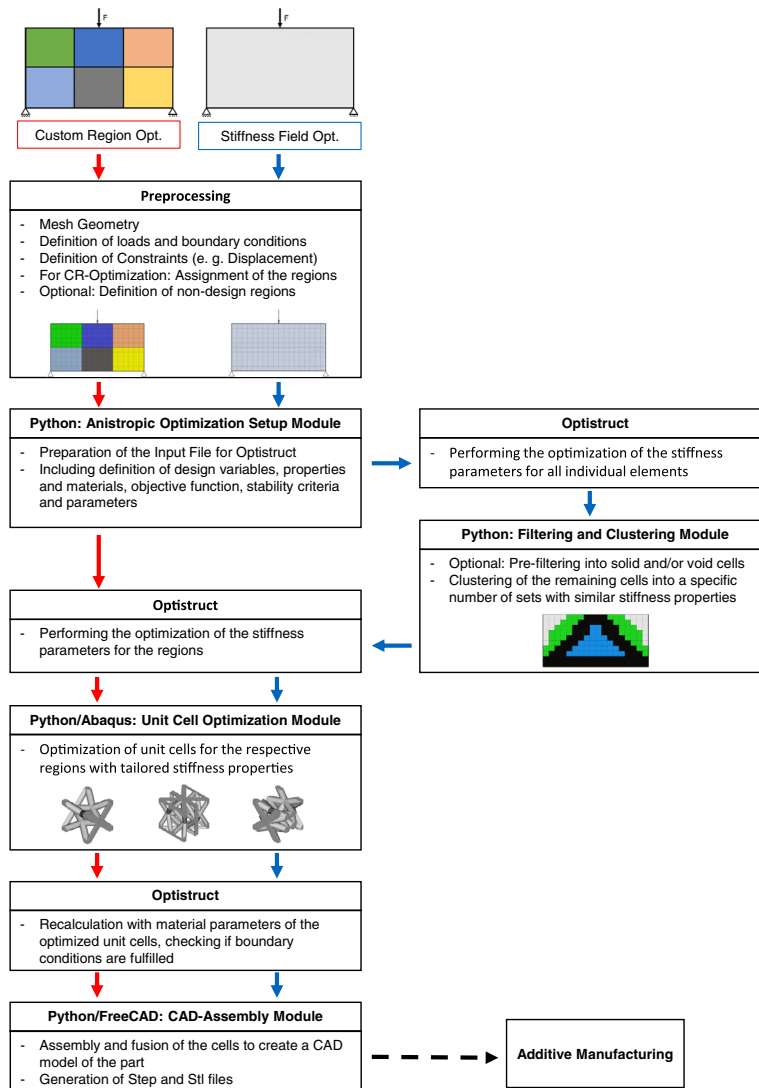


Figure 5. Flowchart of the multiscale lattice design framework.

$$\sum_{i=0}^n \min_{\mu_j \in \mathbb{R}^n} (\|x_i - \mu_j\|^2) \quad (12)$$

The overall design framework is summarized in the workflow of **Figure 5**. The blue arrows represent the flow for the multicell method with the built-in subclustering filter. The fixed custom region method is indicated by the red arrows. If the whole design domain is assigned to one single region, this corresponds to the single-cell approach introduced in Section 2.3.1.

### 3. Results and Discussion

In this chapter, the capabilities and performance of the developed design tool are demonstrated through two 3D static stiffness problems. These problems are solved through various solutions to demonstrate the potential of the developed lattice framework.

#### 3.1. Clamped Beam

The first problem is a 3D beam under pressure on the top surface and torsion on the tip of the beam. The design dimensions and the loading scenario are detailed in **Figure 6**. The FE model is shown in **Figure 7**.

##### 3.1.1. Cell Derivation and Optimization

The single-cell FMO approach of the presented problem converges to the stiffness properties in **Table 1**.

As the next step, the lattice unit structure is designed with the unit cell optimizer with the cell size and truss diameter stated in **Table 2**.

First, the GA is executed to find the best possible topology network. The convergence of the algorithm is plotted in **Figure 8**. With the result of the genetic algorithm, the subsequent PSO searches for the best node positions for the topology of the cell with the best fitness. **Figure 9** shows the evolution of the fitness of the cells during PSO over the generations. It can be seen that the cumulative fitness of the best cells increases and converges very quickly.

The elastic properties of the best design in the GA and the PSO are stated in the second and third rows of **Table 3**. The equivalent solid structure of the optimized cell is constructed with the help of the Python-FreeCAD Tool in order to perform 3D FE analysis through a detailed tetrahedral mesh. The 3D CAD model of the tailored cell can be seen in **Figure 10**. The equivalent properties of the solid-meshed cell are shown in the last row of **Table 3**. This can be treated as the reference homogenized properties with very high accuracy. The overestimation of the beam-meshed model indicates the inaccuracy of the calculation through the developed Timoshenko-beam homogenization framework from Section 2.1.

To achieve the targeted elastic properties derived from the single-cell FMO optimization stated in **Table 1**, slightly higher elastic properties are required. In this article, this is achieved by a simple constant truss diameter upscaling. For this problem, the initially determined  $d_{\text{truss}} = 0.8$  was scaled to  $d_{\text{truss}} = 0.96$  to fulfill both macroscopic stiffness design constraints stated in **Figure 6**.

The final elasticity of the optimized and upscaled lattice structure can be seen in **Table 4**. Due to the deviations of the reduced order Timoshenko beam-based homogenization, the values do not exactly match the targeted metamaterial properties, but the deviations are not significant, and the dominant elastic properties are almost equal to the targeted ones. The infill ratio of the optimized cell is 27%.

##### 3.1.2. Macroassembly of Cells

After the successful derivation of the metamaterial in the form of a lattice unit structure, the design is constructed by filling the unit cells into the 3D design space of the beam problem. This happens with the help of a Python-FreeCAD tool. The design is shown in **Figure 11**.

The constructed lattice assembly was also manufactured with the help of a commercial SLA printer using resin. This demonstrator can be seen in **Figure 12**.

##### 3.1.3. Benchmark with Structures Through Standard Cells

To access the performance of the tailored cells on the presented structural problem, alternative periodic lattice design variants were constructed using some of the well-known standard cells. These structures were designed with equivalent infill as the developed design in **Figure 11**.

The four selected standard cells for the benchmarking are shown in **Figure 13**. All these four standard cells are isotropic, and their elastic properties within the same infill ratio (27%) are listed in **Table 5**.

**Figure 14** indicates the structural performance with respect to the two targeted macroscopic stiffness constraints. It can be seen that the tailored lattice cell exactly matches the required constraints, while the isotropic standard cells fail at least one of the constraints. All of the four benchmarking design variants cannot meet the displacement constraint, suggesting too weak bending stiffness. The optimized cell shows a good performance compared to the listed isotropic standard cells. However, this benchmark is not fully complete, as more advanced anisotropic or diameter-optimized cells could deliver an improved weight-specific stiffness, which may be more similar to the presented tailored cell. Nevertheless, the benefit of the tailored cell compared to the isotropic cells from **Figure 13** is clear and satisfactory.

#### 3.2. Clamped Beam Under Increased Load

Next, the same problem under increased loading is solved. Both the pressure and the torsional moment are doubled, as stated in **Figure 15**.

The optimized metamaterial has the elastic properties shown in **Table 6**. The target stiffness values are doubled compared to the previous problem (**Table 1**) as expected.

##### 3.2.1. Cell Derivation and Optimization

In this analysis, a reduced truss diameter is selected to avoid the deviation between the Timoshenko beam-based approximation



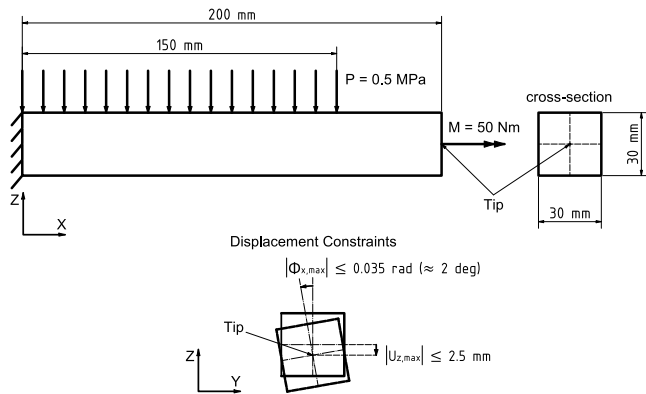


**Figure 6.** The clamped beam problem.

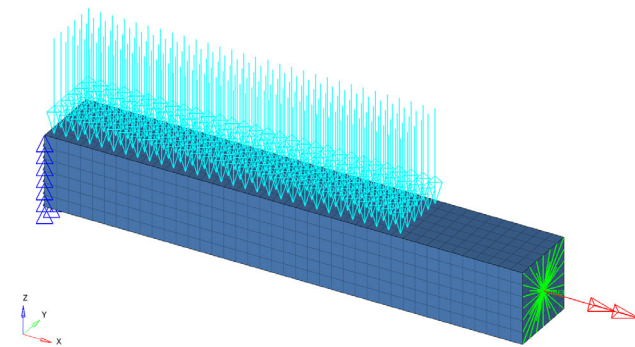


**Figure 7.** The 3D FE model meshed with cubic hexagonal elements.

**Table 1.** Derived material properties for the clamped beam problem.

Variable	$E_1$	$E_2$	$E_3$	$G_{12}$	$G_{23}$	$G_{31}$
Value [MPa]	7896	1000	1068	2451	1000	2555

**Table 2.** Cell dimension settings.

Cell dimensions				
	$R_{\text{Beams}}$	$x_{\text{dim}, \frac{1}{2} \text{Cell}}$	$y_{\text{dim}, \frac{1}{2} \text{Cell}}$	$z_{\text{dim}, \frac{1}{2} \text{Cell}}$
Value [mm]	0.4	2.5	2.5	2.5

and the actual equivalent properties. The most important unit cell properties are summarized in **Table 7**. Also, a higher complexity of the unit cell geometry was set up by the complexity soft constraints of the unit cell optimizer, which allows more complex truss topologies.

As the targeted stiffness properties have a higher magnitude, it would be difficult to directly reach these values within the optimization. For that reason, the ratios between the elastic properties are optimized within the optimization loop, which will be corrected through a posterior truss diameter upscaling.

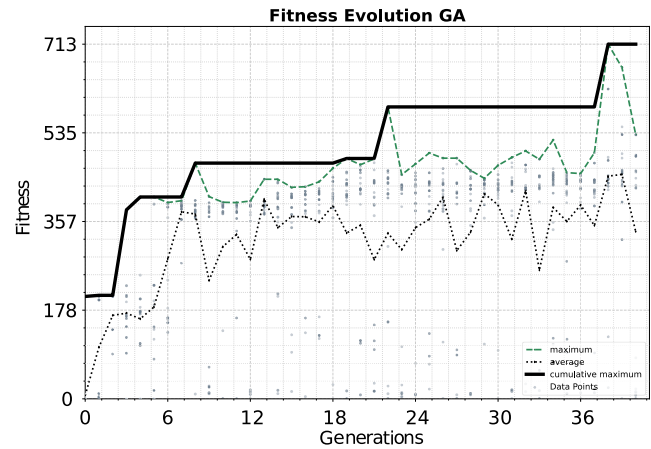


**Figure 8.** Fitness evolution of the targeted unit cell through the genetic algorithm (GA).

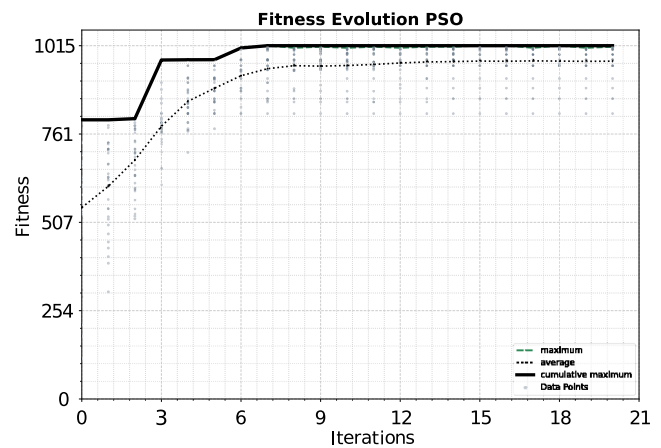


**Figure 9.** Fitness evolution of the targeted unit cell through the PSO algorithm.

**Table 3.** Elastic properties of optimized structures through beam-based and tetra-meshed homogenization.

	$E_1$	$E_2$	$E_3$	$G_{12}$	$G_{23}$	$G_{31}$
Target [MPa]	8000	1000	1100	2700	1000	2700
$GA_{BM, R=0.4 \text{ mm}}$ [MPa]	7177	568	571	2155	2521	2096
$PSO_{BM, R=0.4 \text{ mm}}$ [MPa]	7444	571	574	2128	2524	2063
$PSO_{SM, R=0.4 \text{ mm}}$ [MPa]	5724	462	471	1721	1690	1755

This means that the fitness function of the unit cell tailoring algorithm is formulated according to Equation (2). The targeted ratios for the cost function are summarized in **Table 8**.

The homogenized stiffness properties of the optimized unit cell can be seen in **Table 9**. Due to the modified unit cell settings, there is a good agreement between the prediction of the reduced order beam-based model and the solid reference model. The targeted ratios were achieved pretty well, but the stiffness magnitudes are significantly below the desired values.

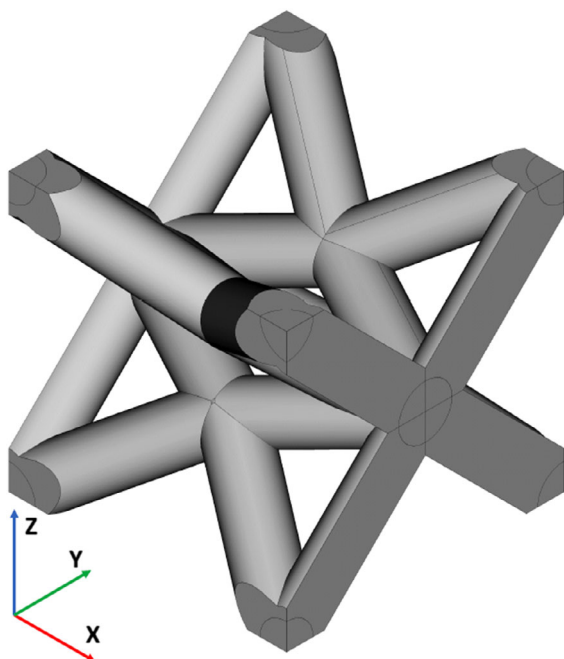


Figure 10. CAD model of the GA-PSO-optimized cell.

Table 4. Elastic properties for the optimized unit cell with an adjusted truss diameter of 0.96 mm.

Variable	$E_1$	$E_2$	$E_3$	$G_{12}$	$G_{23}$	$G_{31}$
Value [MPa]	8876	1052	1088	2613	2633	2676

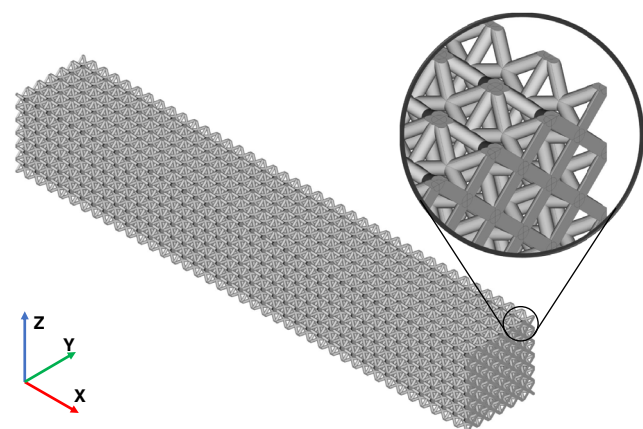


Figure 11. Assembly of unit structures forming the macroscopic design.

For that reason, the truss diameter was scaled up to fulfill the macroscopic stiffness requirements. The final metamaterial properties, after the upscaling, are shown in Table 10. As a result of the upscaling, the optimized ratios do not stay constant, as there is a nonlinear relation between the change of diameter and resulting orthotropic elastic properties. This results in an unnecessarily exaggerated stiffness property in  $y$  and  $z$

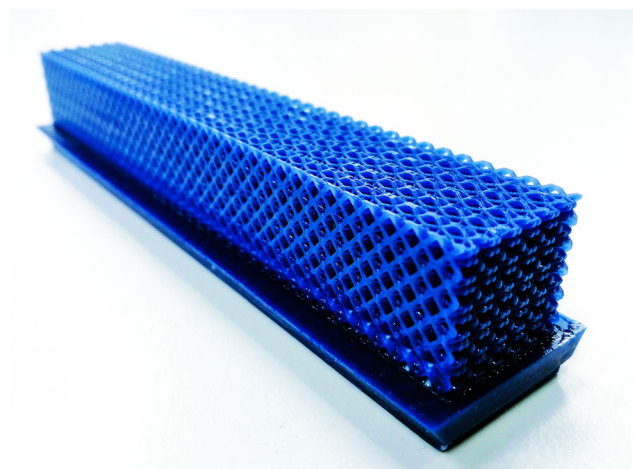


Figure 12. 3D-printed demonstrator of the problem.

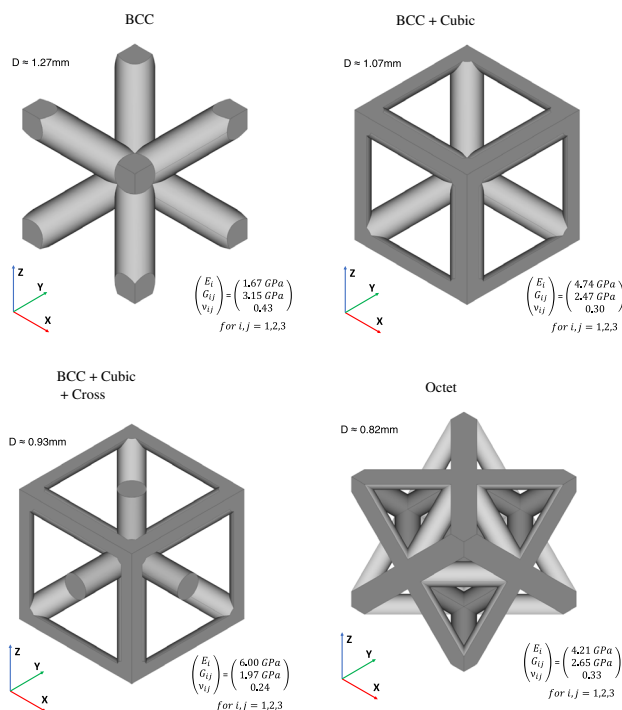


Figure 13. Standard lattice unit cells used for the benchmarking with the optimized unit cell.

directions. This can be seen in the diagram of Figure 16. The optimized cell before and after diameter upscaling can be seen in Figure 17. The infill ratio of the cell is 45%, which is significantly higher than the cell 27%) from the problem under the lower loading from Section 3.1.

### 3.2.2. Macroassembly

The constructed macroscopic structure using the upscaled unit cell is shown in Figure 18. The 3D-printed demonstrator of the



**Table 5.** Diameter and orthotropic material parameters of the benchmark unit cells under investigation.

Var.	BCC	BCC + Cubic	BCC + Cubic + Cross	Octet
$D_{struts}$	1.27 mm	1.07 mm	0.93 mm	0.82 mm
$E_i$	1672 MPa	4742 MPa	6000 MPa	4210 MPa
$G_{ij}$	3154 MPa	2467 MPa	1965 MPa	2648 MPa
$\nu_{ij}$	0.43	0.30	0.24	0.33

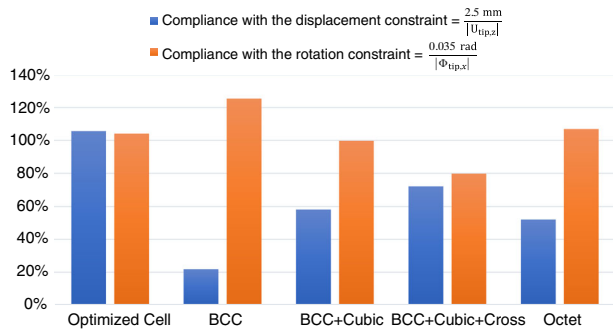


**Figure 14.** Comparison of deformation constraints of the optimized cell against benchmark cells.

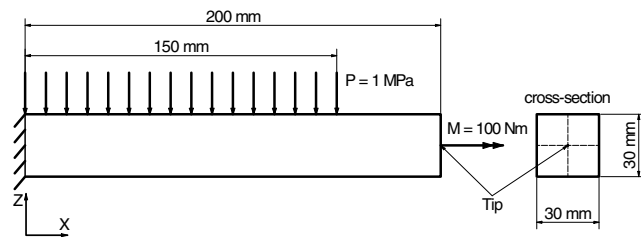


**Figure 15.** The clamped beam under increased load.

**Table 6.** FMO-optimized elastic parameters for the clamped beam under increased loading.

Variable	$E_1$	$E_2$	$E_3$	$G_{12}$	$G_{23}$	$G_{31}$
Value [MPa]	15 564	1137	1070	4701	1000	5526

**Table 7.** Cell dimension settings for increased macroscopic load.

Cell dimensions				
	$R_{Beams}$	$x_{dim, \frac{1}{2} Cell}$	$y_{dim, \frac{1}{2} Cell}$	$z_{dim, \frac{1}{2} Cell}$
Value [mm]	0.25	2.5	2.5	2.5

design problem of the clamped beam with increased load can be seen in **Figure 19**.

This problem of the clamped beam under increased load showed the limitation of the developed lattice framework. The

**Table 8.** Target stiffness ratios of the unit cell for the increased load case.

Target stiffness properties						
Variable	$E_1$	$E_2$	$E_3$	$G_{12}$	$G_{23}$	$G_{31}$
Target [MPa]	15 600	1200	1100	4800	1100	5600
Ratio [–]	1.00	0.08	0.07	0.31	0.07	0.36

**Table 9.** Elastic parameters of the optimized cell with a truss diameter of the initial 0.5 mm.

Variable		$E_1$	$E_2$	$E_3$	$G_{12}$	$G_{23}$	$G_{31}$
Target	Value [MPa]	15 600	1200	1100	4800	1100	5600
	Ratio [–]	1.00	0.08	0.07	0.31	0.07	0.36
Cell <sub>BM, D=0.5 mm</sub>	Value [MPa]	3766	284	520	1161	265	1321
	Ratio [–]	1.00	0.08	0.14	0.31	0.07	0.35
Cell <sub>SM, D=0.5 mm</sub>	Value [MPa]	3192	321	529	1054	258	1032
	Ratio [–]	1.00	0.10	0.17	0.33	0.08	0.32

**Table 10.** Elastic parameters of the optimized cell with the increased truss diameter.

Variable	$E_1$	$E_2$	$E_3$	$G_{12}$	$G_{23}$	$G_{31}$
Value [MPa]	18 347	6780	5119	5743	2156	4300
Ratio [–]	1.00	0.37	0.28	0.31	0.12	0.23

magnitude of the stiffness properties with the initial diameter was below the target metamaterial properties. The applied diameter upscaling distorted the optimized ratios between the elastic properties. For this problem with the increased load, a stiffer base material would be ideal to reduce the need for the diameter upscaling and to preserve the optimized ratios and therefore design the target metamaterial more accurately.

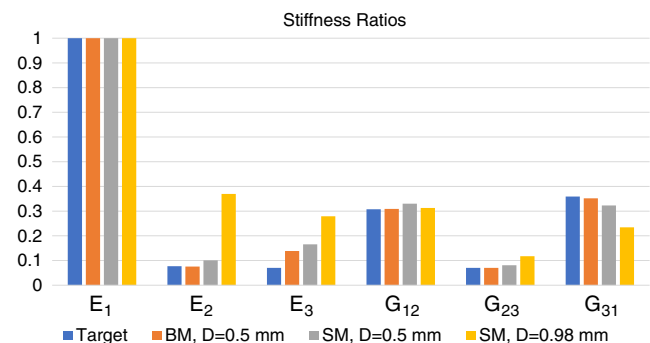


**Figure 16.** Diagram with ratios for the target and the cells with 0.5 and 0.98 mm diameters, calculated with the beam model (BM) and the solid model (SM), respectively.

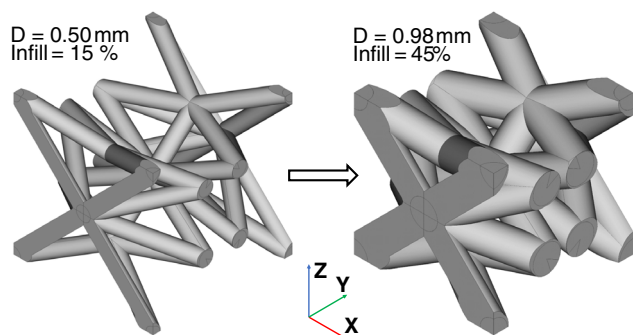


**Figure 17.** Scaling the diameter of the struts in the cell from 0.5 to 0.98 mm to increase the magnitude of elastic properties.

### 3.2.3. Design Through Doubled Unit Cell Size

The posed problem with the increased loading was also solved in a doubled cell size discretization scale as well. In this case, the unit cell dimensions were selected as 10 mm instead of 5 mm, and the truss diameter was similarly doubled ( $d_{\text{truss}} = 1$  mm). The unit cell optimization converged to a very similar topology as the one observed in the previous optimization with the cell size of 5 mm in Section 3.2.1. This serves as a good proof for the repeatability of the optimization and independence of the initial random population of the cell tailoring framework. The lattice assembly using the larger cell is shown in **Figure 20** and **21**. The resulting infill ratio also corresponds to the solution from the smaller unit cell size (45%).

### 3.3. Clamped Beam Through the Multicell Approach

In this use case, the same problem is solved as in Section 3.2, namely the clamped beam under increased loading. The multicell method from Section 2.3.2 is used. For that reason, every finite element within the design space is treated as an independent design variable as in **Figure 22**.

The free-material optimization converged to the elastic property distributions plotted in **Figure 23**. These elastic property fields are used as input for the K-Means filtering to derive four

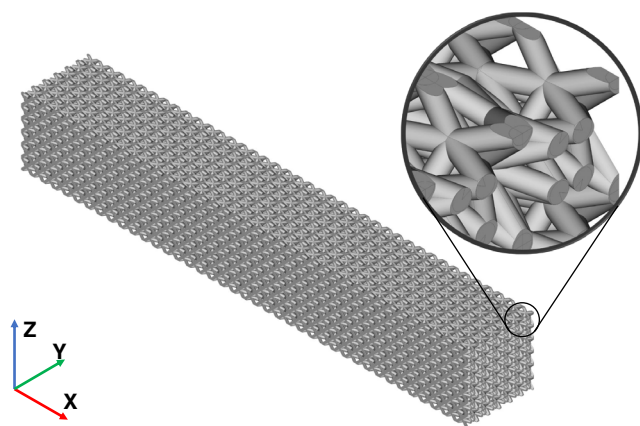


**Figure 18.** Assembly of the tailored lattice cells.

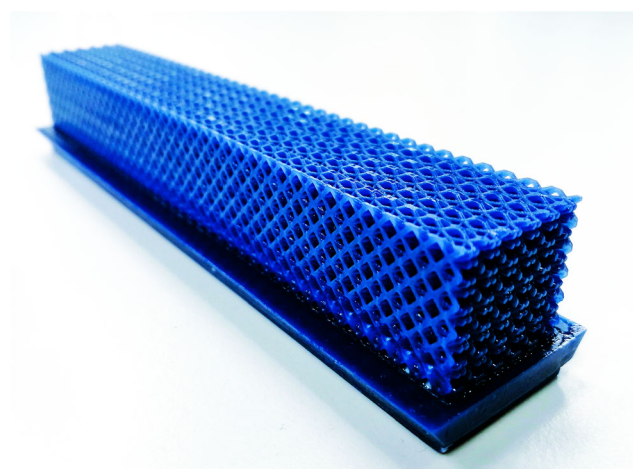


**Figure 19.** 3D-printed demonstrator of the lattice assembly.

subclusters. The filter function was set up to force one of the clusters to be fully filled solid unit. This leads to the distribution of the clusters shown in **Figure 24**.

The three resulting metamaterials are then constructed with the help of the unit cell optimizer. The unit cell dimension and complexity settings are kept constant for these unit cell optimizations. A cell size of 5 mm is used, with a truss diameter of 0.5 mm. Ratio-based optimization is chosen with posterior diameter upscaling. Diameter is kept constant for the three constructed cells. The final unit cells and the corresponding metamaterial properties are summarized in **Figure 25**.

The unit cells were then constructed and merged together with the Python-FreeCAD tool to generate the multicell design assembly, which is shown in **Figure 26**. This figure also reflects the difficulties of stacking the nonuniform adjacent cells together. The 3D-printed demonstrator can be seen in **Figure 27**.

The macroscopic constraints were fulfilled and even showed slightly higher bending stiffness than the single-cell design from Section 3.2. Nevertheless, the overall 45% infill percentage of the design assembly remained the same as in the design solutions

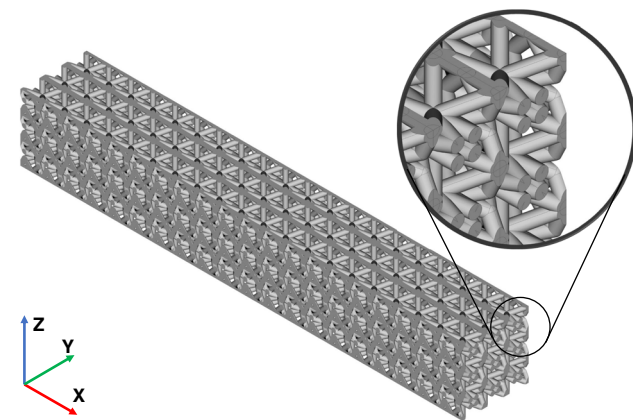


**Figure 20.** Assembly of the double-sized lattice cells for the clamped beam problem under increased load.

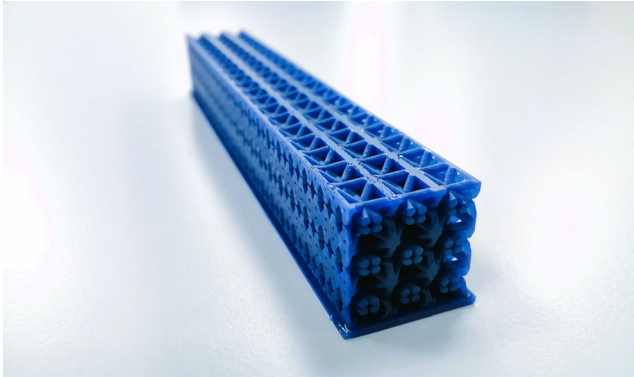


**Figure 21.** 3D-printed demonstrator of the lattice assembly with doubled cell size.

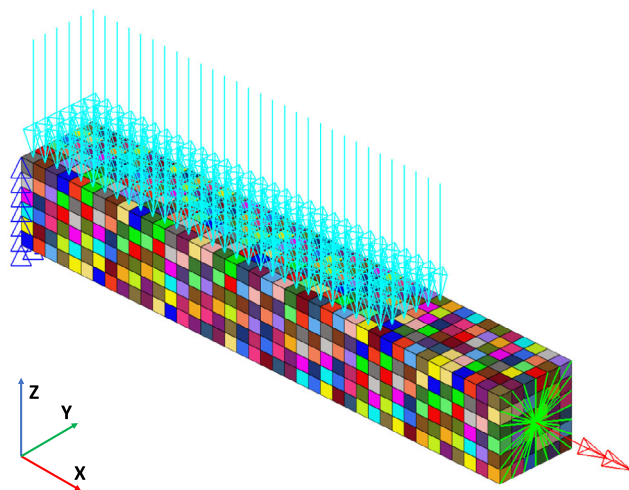


**Figure 22.** Design variables for the clamped beam problem using the multicell method.

based on the single-cell approach in Section 3.2. This means that for this particular use case no lightweight benefit was captured. Using the multicell method may be beneficial for more complex structural problems, where the elastic properties are more distributed within the design space or in case where the single-cell method fails to deliver a sufficiently stiff unit cell to solve the problem.

The workflow and the usability of the multicell method were tested through the design demonstrator in Section 3.3. The multicell design tool shows a robust behavior, even though for this use case no structural or lightweight benefit was observed.

### 3.4. L-Shaped Beam Problem

Finally, a 3D L-shaped problem, which is under a 3D load according to **Figure 28**, is introduced. Single-cell method is applied to find the ideal lattice unit structure to fill the design space. The FE model is shown in **Figure 29**.

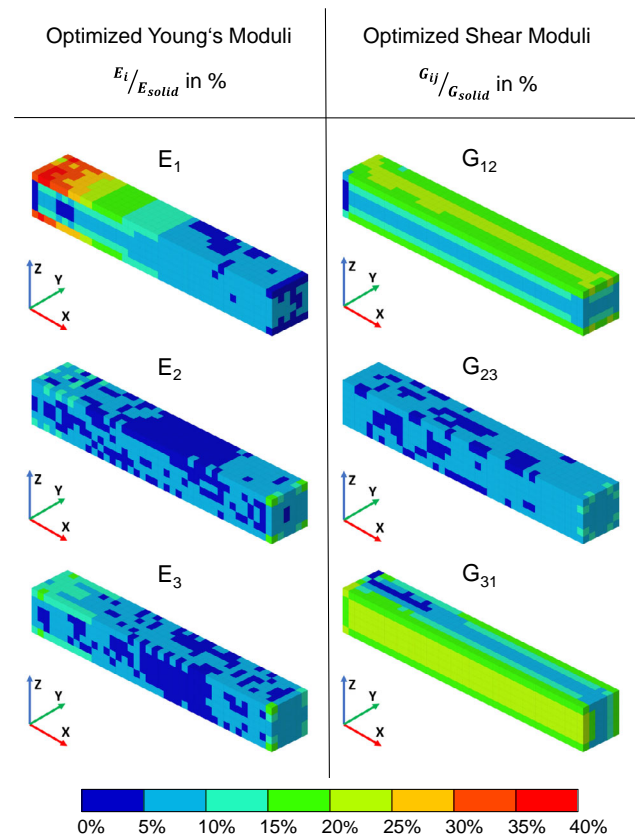


**Figure 23.** Distribution of Young's moduli and shear moduli as a result of multicell free-material optimization (FMO).

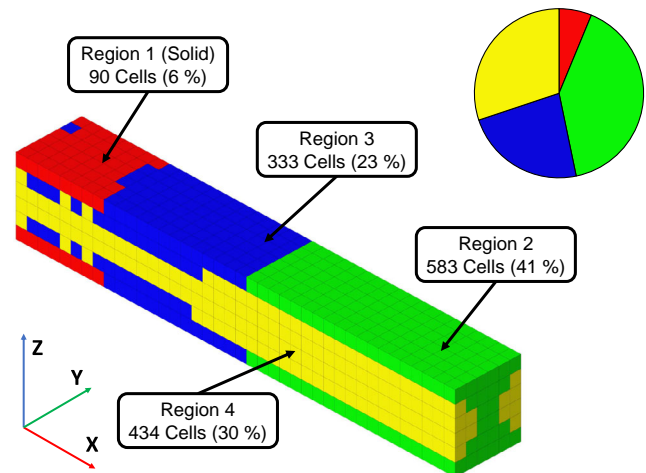


**Figure 24.** Distribution of the elements into four regions as a result of prefiltering and clustering.

The single-cell FMO converges to an orthotropic elastic material, which is used as the target in the unit cell optimizer algorithm. The optimization is carried out as a ratio-based orthotropic stiffness optimization. The targeted material properties and the equivalent properties of the best cell are listed in



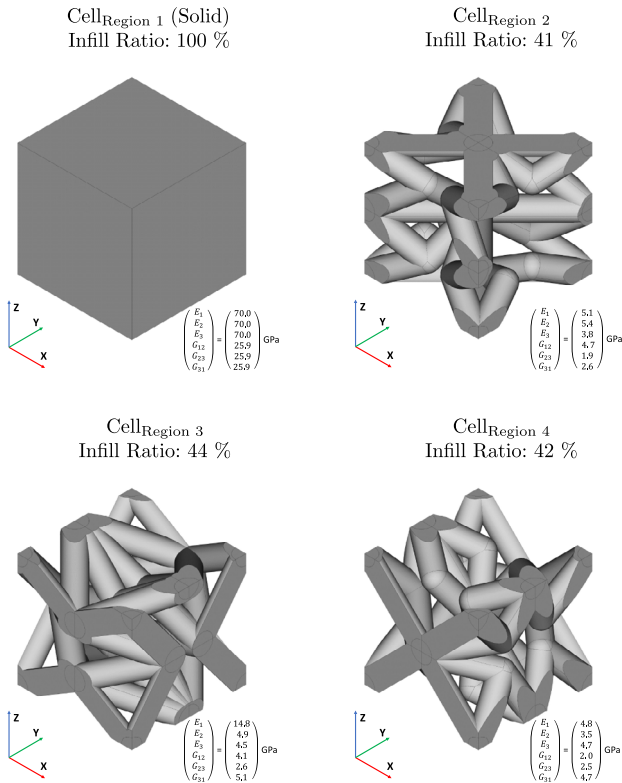


Figure 25. The four different unit cells as a result of the multicell method.

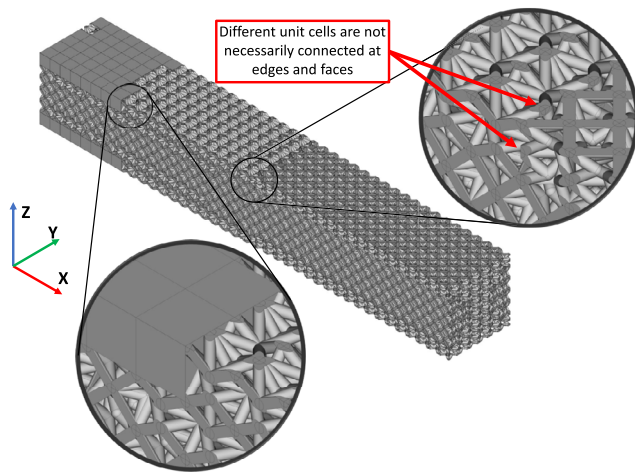


Figure 26. Assembly of the four lattice cells following the multicell approach.

**Table 11.** The optimized ratios approximate the targeted ratios very well, and the relations between the elastic parameters remain similar after the rehomogenization through the detailed tetra mesh. That proves the good approximation of the Timoshenko beam-based homogenization. The magnitudes of the stiffness values are not far from the targeted stiffness values; therefore, a minor diameter upscaling is assumed to be needed.

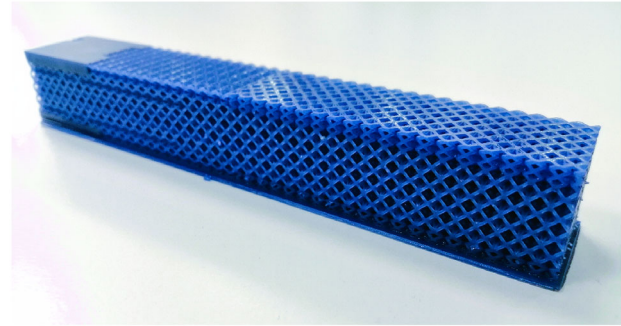


Figure 27. 3D-printed demonstrator of the multicell lattice assembly.

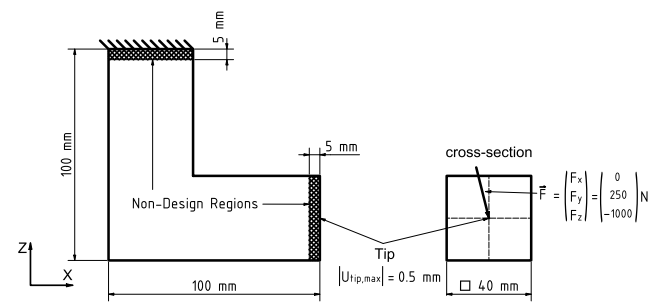


Figure 28. The 3D L-shaped design problem with 3D loading on the tip.

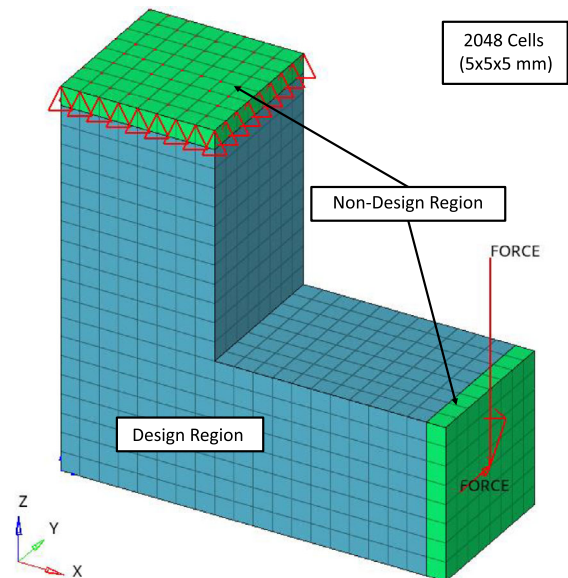
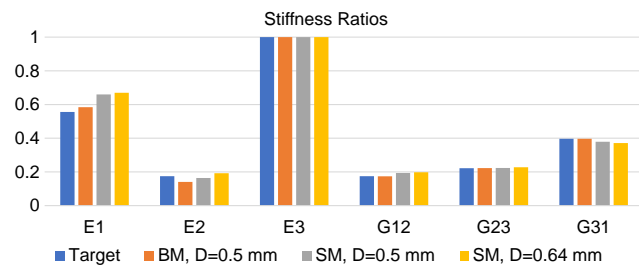


Figure 29. The FE model showing the design space and element size.

The truss diameter was scaled up to  $d_{\text{truss}} = 0.64 \text{ mm}$  to fulfill the stiffness requirements stated in Figure 28. This rather minor upscaling barely changed the optimized stiffness ratios, as shown in Figure 30. Consequently, the resulting elastic stiffness tensor of the metamaterial stays accurate, which leads to

**Table 11.** Elastic parameters of the optimized cell for the L-shaped problem.

Variable		$E_1$	$E_2$	$E_3$	$G_{12}$	$G_{23}$	$G_{31}$
Target	Value [MPa]	3500	1100	6300	1100	1400	2500
	Ratio [-]	0.56	0.17	1.00	0.17	0.22	0.40
Cell <sub>BM,D=0.5 mm</sub>	Value [MPa]	2383	574	4077	710	908	1617
	Ratio [-]	0.58	0.14	1.00	0.17	0.22	0.40
Cell <sub>SM,D=0.5 mm</sub>	Value [MPa]	2559	637	3878	750	868	1469
	Ratio [-]	0.66	0.16	1.00	0.19	0.22	0.38



**Figure 30.** Diagram indicating the ratios for the target material and the cells with 0.5 and 0.64 mm diameter, calculated with the BM and the SM, respectively.

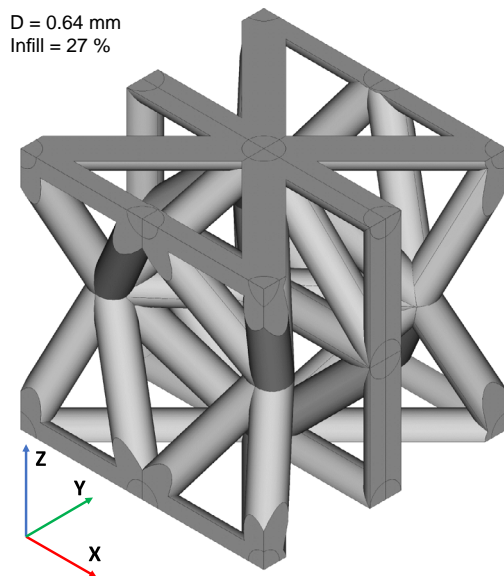


**Figure 31.** CAD model of the optimized cell for the L-shaped design problem.

improved weight saving, when the metamaterial is used to fill the 3D design space.

The final unit cell with the upscaled diameter is shown in **Figure 31**. The infill ratio of the cell is around 27%. The corresponding macrodesign is shown in **Figure 32**. The problem of the 3D L-shaped beam, solved through the developed single-cell lattice tool, showed good performance. As the global stiffness

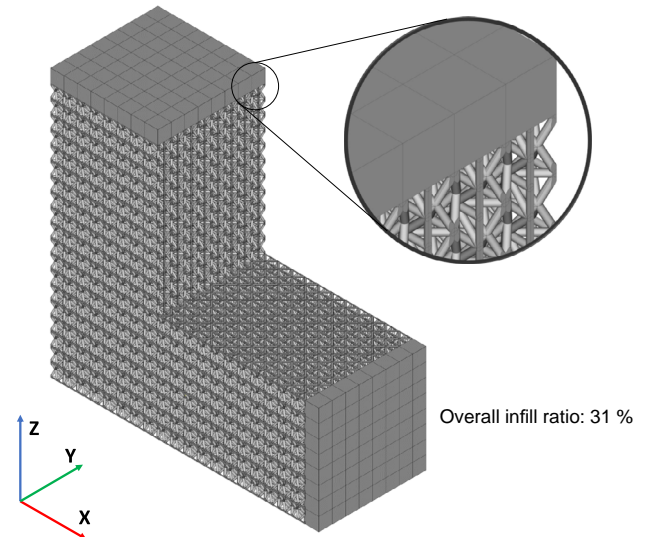


**Figure 32.** Assembly of the optimized lattice cell for the L-shaped problem following the single-cell approach.

constraints were not so strict as in Section 3.2 for the clamped beam problem, the used base material ( $E_{ref} = 70000$  MPa) was sufficiently stiff to construct a well-performing unit cell, whereas only a minor posterior diameter modification was required to fulfill the global structural requirements. In contrast, the clamped beam under the increased load was harder to solve with the same base material and beam slenderness setting, as a significantly stiffer metamaterial was targeted. The cell was realized with a good infill rate of 27%.

## 4. Conclusion

### 4.1. Summary

In this work, a periodic lattice design tool that first derives the ideal elastic material properties of the 3D stiffness problem through the FMO algorithm is presented. Subsequently, the developed unit cell optimizer is used to construct the best topology for reaching that orthotropic target material. The optimizer uses a population-based algorithm evaluating the elastic properties of the cell individuals through a reduced-order Timoshenko beam-based calculation framework. The tailored cells are then used to design the macroscopic component by filling the domain with the unit cells. Single-cell and multicell filling methods were developed to construct the macroscopic component.

These methods were demonstrated through multiple use cases, where the elasticity of the printing material was fixed. The clamped beam under reduced load was solved easily with the single-cell approach. The developed lattice design was benchmarked against a few alternative lattice designs using standard cells. All these standard design solutions were outperformed by the developed lattice cell in terms of structural lightweight performance. The same problem under double loading was also solved, showing more difficulty in cell construction due to the higher stiffness requirements of the metamaterial. The same



3D domain was also solved through the multicell approach. The design workflow worked smoothly, but for this use case, a lightweight benefit was not captured. Finally, the L-shaped beam problem was presented through the single-cell method showing smooth workflow and good design performance.

## 4.2. Outlook

The developed design tool was presented for linear elastic lightweight problems. Nevertheless, lattice structures have a good potential for attractive energy absorption properties as well. The developed framework is extendable to other quantifiable structural properties such as unidirectional strength and energy absorption, enabling crashworthiness as an objective on the macroscale to be considered. The evaluation of such nonlinear unit cell responses is more difficult and requires future work; moreover, further nonstructural design responses could be added to the framework to target the development of a multifunctional metamaterial.

The integration of other nonstructural responses, such as wave propagation or thermal properties, might also be possible. Such an approach would enable a compact multidisciplinary formulation of the metamaterial optimization through truss-like lattice cells. In this article, simple isotropic elastic printing material was considered, and no process-induced effect on the printed material was analyzed. In reality, printed material is affected by imperfections of manufacturing technology. Nevertheless, such a modified 3D-printed material card could be easily added to the unit cell homogenization framework. Due to the various geometric constraints of the unit cell optimizer algorithm, printability design constraints could be also defined in the population-based cell tailoring algorithm. In this article, all these functionalities were deactivated, as the exploration of the capabilities of the design method was in focus.

## Compliance with Ethical Standards

Replication of results: The authors wish to withhold the code for commercialization purposes. This includes the Abaqus–Python framework of microscale simulations and the python code implementing the optimization.

## Acknowledgements

This research was supported by the Bavarian Ministry of Economic Affairs, Regional Development, and Energy.

Open Access funding enabled and organized by Projekt DEAL.

## Conflict of Interest

The authors declare no conflict of interest.

## Data Availability Statement

The data that support the findings of this study are available from the corresponding author upon reasonable request.

## Keywords

design, lattice, metamaterial, multiscale, optimization, structural

Received: September 21, 2022

Revised: October 26, 2022

Published online: November 28, 2022

- [1] P. Singh, in *Studies in Computational Intelligence* (Eds: H. Malik, A. Iqbal, P. Joshi, S. Agrawal, F. I. Bakhsh, Vol. 916, Springer Singapore, Singapore **2021**, pp. 3–33.
- [2] O. Kramer, in *Genetic Algorithm Essentials*, Vol. 679, Springer International Publishing, Cham **2017**.
- [3] J. Tao, R. Zhang, Y. Zhu, in *DNA Computing Based Genetic Algorithm*. Springer Singapore, Singapore **2020**.
- [4] B. Vaissier, J.-P. Pernot, L. Chougrani, P. Véron, *Comput-Aid. Des.* **2019**, *110*, 11.
- [5] M. P. Bendsoe, O. Sigmund, in *Topology Optimization: Theory, Methods and Applications*, Vol 2, Springer, Berlin **2003**.
- [6] G. Allaire, F. Jouve, A.-M.: Toader, *J. Comput. Phys.* **2004**, *194*, 363.
- [7] D. Chen, M. Skouras, B. Zhu, W. Matusik, *Sci. Adv.* **2018**, *4*, 7005.
- [8] L. Xia, P. Breitkopf, *Struct. Multidiscipl. Optim.* **2015**, *52*, 1229.
- [9] O. Sigmund, *Int. J. Solids Struct.* **1994**, *31*, 2313.
- [10] S. Pantelakis, K. Tserpes, in *Revolutionizing Aircraft Materials and Processes*, Springer Nature, Switzerland **2020**.
- [11] M. F. Ashby, *Philos. Trans. Ser. A, Math. Phys. Eng. Sci.* **2006**, *364*, 15.
- [12] L. J. Gibson, M. F. Ashby, *Cellular Solids*, Cambridge University Press, Cambridge **1997**, pp. 52–92.
- [13] S. Arabnejad, D. Pasini, *Int. J. Mech. Sci.* **2013**, *77*, 249.
- [14] D. Marschall, H. Rippl, F. Ehrhart, M. Schagerl, *Mater. Des.* **2020**, *190*, 108539.
- [15] G. Dong, Y. Tang, Y. F. Zhao, *J. Mech. Des.* **2017**, *139*, 100906.
- [16] H. Tollenaere, D. Caillerie, *Adv. Eng. Softw.* **1998**, *29*, 699.
- [17] F. Dos Reis, J. F. Ganghoffer, *Tech. Mechanik* **2010**, *30*, 85.
- [18] A. Vigliotti, D. Pasini, *Mech. Mater.* **2012**, *46*, 57.
- [19] A. Vigliotti, D. Pasini, *Comput. Methods Appl. Mech. Eng.* **2012**, *229–232*, 27.
- [20] A. Vigliotti, V. S. Deshpande, D. Pasini, *J. Mech. Phys. Solids* **2014**, *64*, 44.
- [21] S.-I. Park, D. W. Rosen, *J. Mech. Des.* **2018**, *140*, 111414.
- [22] X. Zhang, S. Maheshwari, A. S. Ramos, G. H. Paulino, *J. Struct. Eng.* **2016**, *142*, 04016090.
- [23] R. Su, L. Gui, Z. Fan, in *Fifth Inter. Conf. on Natural Computation*, IEEE, Piscataway, NJ **2009**, pp. 485–491.
- [24] M. Giger, P. Ermanni, *Struct. Multidiscipl. Optimiz.* **2006**, *32*, 313.
- [25] M. Bujny, N. Aulig, M. Olhofer, F. Duddeck, *Int. J. Crashworth.* **2018**, *23*, 395.
- [26] M. Bujny, N. Aulig, M. Olhofer, F. Duddeck, *GECCO '18 Proc. Genet. Evol. Comput. Conf.*, Association for Computing Machinery, New York, NY **2018**, pp. 825–832.
- [27] E. Raponi, M. Bujny, M. Olhofer, N. Aulig, S. Boria, F. Duddeck, *Comput. Methods Appl. Mech. Eng.* **2019**, *348*, 730.
- [28] E. Raponi, M. Bujny, M. Olhofer, S. Boria, F. Duddeck, *Proc. 11th Int. Joint Conf. Comput. Intell.*, SCITEPRESS-Science and Technology Publications, LdaSetubal, Portugal **2019**, pp. 70–81.
- [29] U. T. Ringertz, *Struct. Multidiscipl. Optimiz.* **1993**, *5*, 265.
- [30] M. P. Bendsoe, J. M. Guedes, R. B. Haber, P. Pedersen, J. E. Taylor, *J. Appl. Mech.* **1994**, *61*, 930.
- [31] M. P. Bendsoe, O. Sigmund, in *Topology Optimization: Theory, Methods, and Applications*, 2. Ed., Corrected Printing Edn. *Engineering Online Library*, Springer, Berlin and Heidelberg **2004**.
- [32] J. Zowe, M. Kočvara, M. P. Bendsoe, *Math. Program.* **1997**, *79*, 445.

- [33] J. Zowe, *Mathematics — Key Technology for the Future* (Eds: W. Jünger, H.-J. Krebs), Springer Berlin Heidelberg, Berlin, Heidelberg **2003**, pp. 573–583.
- [34] A. G. Weldeyesus, M. Stolpe, *Comput. Optimiz. Appl.* **2015**, *61*, 409.
- [35] C. Imediegwu, R. Murphy, R. Hewson, M. Santer, *Struct. Multidiscipl. Optimiz.* **2019**, *60*, 513.
- [36] A. Ferrer, J. Oliver, J. C. Cante, O. Lloberas-Valls, *Adv. Model. Simul. Eng. Sci.* **2016**, *3*, 23.
- [37] C. Pan, Y. Han, J. Lu, *Appl. Sci.* **2020**, *10*, 6374.
- [38] R. M. Gorguluarslan, U. N. Gandhi, Y. Song, S.-K. Choi, *Rapid Prototyp. J.* **2017**, *23*, 305.
- [39] M. Nightingale, R. Hewson, M. Santer, *Struct. Multidiscipl. Optimiz.* **2021**, *63*, 1187.
- [40] L. Xia, P. Breikopf, *Comput. Meth. Appl. Mech. Eng.* **2015**, *286*, 147.
- [41] B. Zhu, M. Skouras, D. Chen, W. Matusik, *ACM Trans. Graph.* **2017**, *36*, 120b.
- [42] S. L. Omairey, P. D. Dunning, S. Sriramula, *Eng. Comput.* **2019**, *35*, 567.
- [43] A. G. Weldeyeus, DTU Wind Energy PhD: Models and Methods for Free Material Optimization, **2014**
- [44] F. Pedregosa, G. Varoquaux, A. Gramfort, V. Michel, *J. Machine Learn. Res.* **2011**, *12*, 2825.